nature nanotechnology

ARTICLES

https://doi.org/10.1038/s41565-022-01099-z

Light-driven microdrones

Xiaofei Wu[1,2]✉, Raphael Ehehalt[1], Gary Razinskas[1,3], Thorsten Feichtner[1], Jin Qin[1] and Bert Hecht[1]✉

When photons interact with matter, forces and torques occur due to the transfer of linear and angular momentum, respectively. The resulting accelerations are small for macroscopic objects but become substantial for microscopic objects with small masses and moments of inertia, rendering photon recoil very attractive to propel micro- and nano-objects. However, until now, using light to control object motion in two or three dimensions in all three or six degrees of freedom has remained an unsolved challenge. Here we demonstrate light-driven microdrones (size roughly 2 μm and mass roughly 2 pg) in an aqueous environment that can be manoeuvred in two dimensions in all three independent degrees of freedom (two translational and one rotational) using two overlapping unfocused light fields of 830 and 980 nm wavelength. To actuate the microdrones independent of their orientation, we use up to four individually addressable chiral plasmonic nanoantennas acting as nanomotors that resonantly scatter the circular polarization components of the driving light into well-defined directions. The microdrones are manoeuvred by only adjusting the optical power for each motor (the power of each circular polarization component of each wavelength). The actuation concept is therefore similar to that of macroscopic multirotor drones. As a result, we demonstrate manual steering of the microdrones along complex paths. Since all degrees of freedom can be addressed independently and directly, feedback control loops may be used to counteract Brownian motion. We posit that the microdrones can find applications in transport and release of cargos, nanomanipulation, and local probing and sensing of nano and mesoscale objects.

Light-induced forces promise numerous fascinating technological and scientific applications such as manipulation of atoms[1–3], optical tweezers[4,5], cavity-optomechanics[6] and even solar sails[7]. The resulting accelerations are small for macroscopic objects but become quite large for microscopic objects with small masses. For example, a moderate light flux of around 1 mW μm^{-2} can create a deflection force of about 50 fN for an object with a 10^4 nm^2 absorption cross section. For objects with masses on the order of 1 pg, this force results in strong accelerations of about 50 m s^{-2}. Using photon recoil to actuate microscopic objects is therefore very attractive[8–10].

Although basic motions, such as unidirectional translation[11–15] and rotation[16–24], of objects driven by optical forces have been realized in various instances for quite some time, most of these experiments lack true control of the motion, since the actuations are limited to only one or even half a degree of freedom. Optical tweezers[5] can be used to manipulate objects in a well-controlled manner using light. In optical tweezers, particles are trapped in strongly focused light fields and can be moved by changing the position of the focus. The orientation of objects typically remains uncontrolled unless special particle shapes are combined with linearly polarized light[25] or several bulky handles are controlled using multi-beam optical traps[26–29]. Alternatively, orientation control or rotation of nano-objects can also be achieved via transfer of spin[16–21] or orbital angular momentum[22–24,30]. Nevertheless, the fact that optical tweezers rely on gradient forces poses some limitations. In particular, the gradient force strongly depends on the size and shape of the trapped particle, the displacement of the particle from the focus centre and the refractive index contrast between the particle and the environment. Moreover, the light field gradient is restricted by the diffraction limit of the focus, which hinders stiff trapping for nanoscale particles. Therefore, usually a very high light intensity has to be used to obtain a sufficiently stable and accurate trap. Although near-field optical tweezers[31] can overcome these drawbacks to some degree, they are typically fixed on a substrate and thus not suitable for steering objects.

Using focused light can be avoided if the objects absorb or scatter light asymmetrically in either longitudinal or transverse directions with respect to the propagation direction of the light, causing unbalanced recoil forces[14,15,32–38]. Plasmonic nanoantennas[39] are very well suited for such a purpose, as they can efficiently absorb or scatter light with a well-defined directionality to generate thrust forces, and thus can act as motors if they are integrated into a rigid matrix. Moreover, plasmonic nanoantennas can also be designed to interact resonantly with different degrees of freedom of light, for example wavelength as well as spin and orbital angular momentum, such that it is possible to address them individually even when using unfocused light. Tanaka et al.[15] reported asymmetric plasmonic dimer antennas that could generate lateral optical forces by scattering incident light to one specific transverse direction. When an array of identical antennas with the same orientation or four identical antennas with orientations rotating in 90° steps were arranged in a microblock and illuminated with linearly polarized light, they could produce unidirectional translation or unidirectional rotation, respectively. As no reverse motion was possible, the actuation only covered half a degree of freedom. Besides, optical trapping was still used to confine the object in a line for the translation or in a spot for the rotation. Other photonic structures can also produce asymmetric scattering but typically have larger sizes. Andrén et al.[35] used unidirectional scattering of a large array of scatterers—a so-called metasurface—to drive a comparatively large object moving forwards and transfer of angular momentum of circularly polarized light to make the object turn to the right or left. Unfocused illumination was used in the experiments. As no reverse motion was possible either and the turning was always combined with forwards translation with a constant radius, the actuation was limited to one and a half non-independent degrees of freedom: the maximum that

[1]Nano-Optics and Biophotonics Group, Experimental Physics 5, Institute of Physics, University of Würzburg, Würzburg, Germany. [2]Present address: Leibniz Institute of Photonic Technology, Jena, Germany. [3]Present address: Department of Radiation Oncology, University of Würzburg, Würzburg, Germany. ✉e-mail: xiaofei.wu@physik.uni-wuerzburg.de; hecht@physik.uni-wuerzburg.de

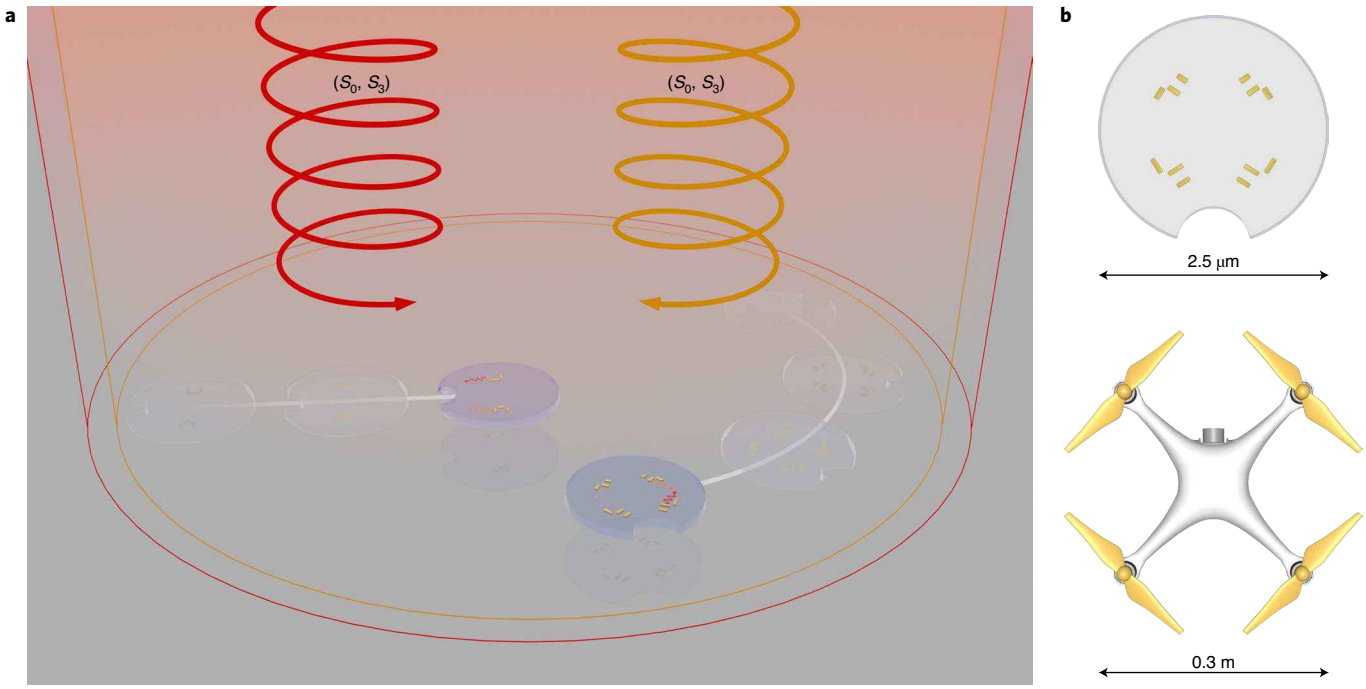

Fig. 1 | Illustration of the setup and microdrone actuation concept. a, Two unfocused light beams of different wavelengths (orange, 830 nm and red, 980 nm) are used to steer microdrones (four- and two-nanomotor devices) by adjusting the laser power and the polarization state, that is, S_0 and S_3 of the Stokes parameters, of each beam. Gold nanoantennas integrated into the transparent body of the microdrone are resonantly excited by either of the two wavelengths and a certain circular polarization, and then scatter light into defined lateral directions (indicated by the small wavy arrows), which leads to corresponding effective optical recoil forces. Perfect 2D motion is achieved by means of the light pressure in propagation direction that pushes the microdrones towards the substrate, while sticking is avoided due to same surface charges on the microdrones and the substrate. **b**, The top view of the four-motor microdrone (top) and comparison to a macroscopic quadcopter drone (bottom). The body of the microdrone is a circular disc with a diameter of 2.5 μm and thickness of 200 nm. The notch of the body indicates the orientation. Despite the tremendous difference in size, the motor configuration (two pairs of motors with opposite chirality) and steering principles (by only adjusting the power of each control channel) are very similar.

could be achieved up to date for light-driven microscopic objects with unfocused illumination. The limitation of control degrees of freedom and systematic steering for these objects comes from the fact that they either have only one motor or have identical motors that cannot be addressed individually.

Here we demonstrate light-driven microdrones with full control of all three independent degrees of freedom in two-dimensional (2D) motions: that is, forwards–backwards and left–right translations and clockwise (CW)–counterclockwise (CCW) rotation. Figure 1a shows a sketch of two microdrones being steered along arbitrary trajectories in two dimensions by two unfocused laser fields at 830 and 980 nm wavelengths. The microdrones contain either two or four plasmonic nanomotors integrated into a rigid transparent body and symmetrically arranged with respect to the centre of the body. Although they are very close to each other, on the order of the used wavelengths, the nanomotors can be individually addressed by means of a wavelength-dependent, chiral response to the circular polarization components of the light[37,38]. The two wavelengths and two circular polarization components provide a maximum of four independent control channels. It is therefore possible to use unfocused illumination with moderate intensities (in contrast to optical tweezers), which circumvents the need for adjusting the light beam positions to follow the microdrone. Note that in previously reported studies, linear polarizations of the excitation light were the effective components for creating photon recoil forces and translations, while circular polarizations were only used for creating torques and rotations. For the present microdrones, by contrast, the circular polarization components are responsible for all forces and torques and therefore for both translational and rotational motions. The advantage of using circular polarization components lies in their continuous rotational symmetry, such that the nanomotors' response is independent of the microdrone's in-plane orientation. As a result, only adjusting the optical power for each motor, that is, the power of each circular polarization component of each wavelength by controlling the total power and polarization states (Stokes parameters S_0 and S_3, respectively), is required to steer the microdrones, such that the steering mechanism is very much simplified. The actuation concept is therefore very similar to that of macroscopic multirotor drones that can accomplish complex manoeuvres[40,41]. Figure 1b highlights the similarity between the four-motor microdrone in the present work and a macroscopic quadcopter drone, each containing two pairs of individually addressable motors with opposite chirality but differing five orders of magnitude in size. For the experimental implementation of the microdrones, we have developed unique nanofabrication techniques. In particular, high-precision single-crystalline plasmonic nanomotors are fabricated using an efficient focused helium ion beam milling method.

Principle of plasmonic nanomotors and microdrones

The concept of the microdrone motors is based on the idea of using the helicity of light to switch the near-field intensity distribution of plasmonic nanostructures. The nanomotor design starts from a plasmonic core element consisting of two identical nanorods perpendicular to each other (Fig. 2a middle column)[42]. This core element takes advantage of an equal-amplitude superposition of a symmetric and an antisymmetric mode of the weakly coupled nanorod pair such that the near field on either of the two nanorods is completely cancelled depending on the circular polarization of

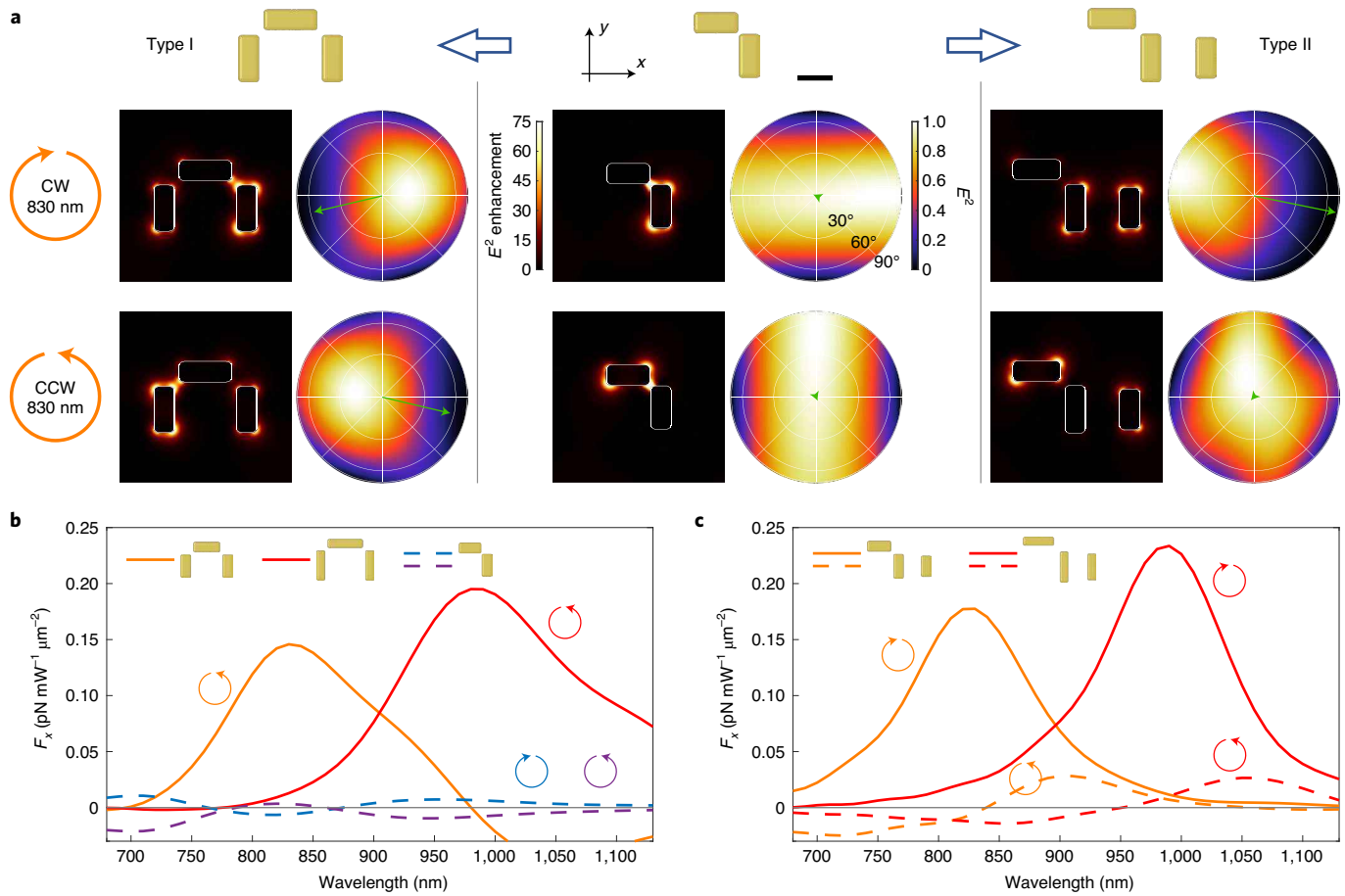

Fig. 2 | Working principle of plasmonic nanomotors (simulation). a, Two types of nanomotor (left and right columns) are developed by adding an additional gold nanorod to a core element (middle column) consisting of two identical orthogonal gold nanorods. The additional nanorod serves as a reflector and together with the vertical nanorod of the core structure leads to a directional scattering once the vertical rod is excited. The structures are designed to work at 830 nm wavelength. The near-field intensity distribution (left panel) and far-field angular distribution of the scattered intensity (right panel, normalized to maximum) are displayed for each column and each circular polarization. The scale bar (100 nm) and colour bars in the middle column apply to all three columns. The green arrows superimposed onto the scattering patterns represent the total force in the *xy* plane, with a linearly scaled length denoting the magnitude of the force. The force corresponds to 0.18 pN mW^{-1} μm^{-2} when the arrowhead reaches the 90° ring of the scattering pattern. **b**,**c**, The major force component F_x as a function of the excitation wavelength and circular polarization for the type-I motors working at 830 or 980 nm and the core element working at 830 nm (**b**), and the type-II motors working at 830 or 980 nm (**c**), demonstrating the distinct wavelength- and circular polarization-dependent response of the nanomotors. For the type-I motors, only the spectra of F_x for CCW are plotted due to symmetry. The excitation light source is a plane wave incident along the *z* direction.

the excitation light, as seen in the middle column of Fig. 2a. To provide lateral thrust, the core element is combined with an additional plasmonic nanorod that acts as a reflector element, similar to Yagi–Uda antennas, and results in a directional light scattering. Using this concept, we have implemented two different configurations that differ in the position of the reflector element, as depicted in Fig. 2a (type I, left column and type II, right column). For both configurations, the lengths of all the nanorods and their distances are further optimized to achieve the best performance. The symmetric motor (type I) produces the same lateral thrust in opposite directions for both circular polarizations. The asymmetric motor (type II) produces lateral thrust only for CW polarization, while for CCW polarization no lateral force is produced due to a symmetric scattering pattern. Note that the core element alone does not provide any directional scattering and therefore no lateral force is produced. For both motor types, we take advantage of the tunability of plasmonic resonances to construct two different versions that are resonant at 830 and 980 nm, respectively. Figure 2b,c displays the respective spectra of force component F_x (for F_y see Supplementary Fig. 1) for both circular polarizations. We obtain peak lateral forces of up to 0.23 pN mW^{-1} μm^{-2} with contrast ratios >10 between the two wavelengths (both type I and II) and >30 between the two circular polarizations (type II). The very small cross talk means that these nanomotors can be controlled individually by circular polarization components of light with the respective wavelength. A general discussion of force efficiencies of the nanomotors is presented in Supplementary Note 1.

On the basis of these properties, the two types of nanomotor working at wavelengths of 830 and 980 nm are used to construct two types of microdrone, one consisting of two type-I motors (two-motor microdrone) and the other one consisting of two pairs of type-II motors with opposite chirality (four-motor microdrone), as shown in Fig. 3. Because each of the nanomotors can be addressed individually, with the combinations of wavelength and circular polarization listed in the upper row of Fig. 3, the two-motor microdrone can be actuated in two degrees of freedom (forwards–backwards translation and rotation), while the four-motor microdrone even offers one additional degree of freedom (right–left

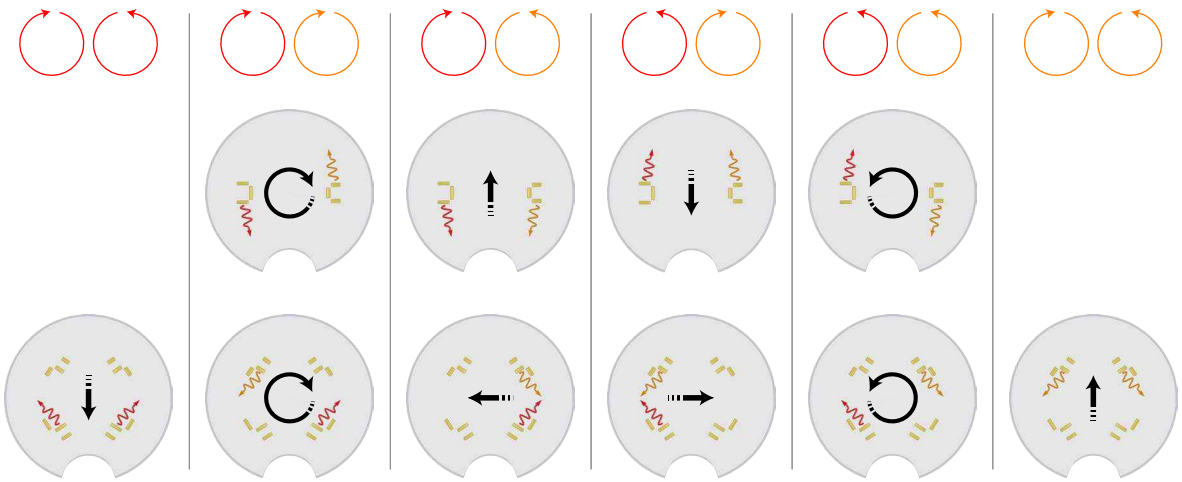

Fig. 3 | Sketches of fundamental actuation patterns for two- and four-motor microdrones. The top row shows the different combinations of the two wavelengths (830 nm in orange and 980 nm in red) and two circular polarizations (denoted by the circular arrows) for realizing the fundamental degrees of freedom for the two- or four-motor microdrones, respectively (second and third rows, respectively). Translation or rotation directions are denoted by the black arrows. The resonant plasmonic nanomotors scatter light of certain wavelengths and certain circular polarization into different directions (indicated by the wavy arrows), and the microdrones are therefore driven by the resulting overall recoil forces and torques.

translation), as illustrated by the black arrows. To achieve rotations (translations), the two colours (830 and 980 nm) should have the same (opposite) circular polarizations, such that the resulting forces (torques) have opposite directions and can be cancelled by adjusting the power ratio of the two colours. It is noticed that for each nanomotor, in addition to the torque of $\boldsymbol{r}\times\boldsymbol{F}$, where $\boldsymbol{r}$ is the position vector of the mass centre of the motor with respect to the centre of the microdrone and $\boldsymbol{F}$ is the total force in the xy plane (Fig. 2a), there is also a non-zero torque with respect to the mass centre of the motor (Supplementary Fig. 2), which is a result of transfer of spin angular momentum of photons[21]. For the motor configurations in Fig. 3, these two torque components of each motor add up constructively since they always have the same direction. The effect of the torque component resulting from transfer of spin angular momentum for different motor configurations is further investigated in Supplementary Video 1.

Device fabrication

The structures fabricated for the experimental demonstration of microdrones are displayed in Fig. 4. The correct dimensions of the gold nanorods that constitute the nanomotors are verified by measuring the far-field angular distribution of the scattering for the type-I motor working at 830 nm. The spectrum of F_x extracted from the measured scattering patterns at varying wavelengths agrees well with the simulation (Supplementary Fig. 3). Fabrication details are described in the Methods section and Extended Data Figs. 1–3. Briefly, in the first step, the gold nanomotors are fabricated on a hydrogen silsesquioxane (HSQ) layer on a substrate coated with indium tin oxide (ITO) by means of focused helium ion beam milling of a single-crystalline gold flake with an efficient outline milling and gold flake peeling method (Fig. 4a–c). Due to the high-quality gold material[43] and the high resolution of the helium ion beam, the resulting structures exhibit accurate and consistent geometries, which ensures quantitative agreement between experiment and simulation (Supplementary Fig. 3). In the next step, the transparent microdrone bodies (made of HSQ) are created (Fig. 4d,e). The HSQ body, in which the nanomotors are encapsulated, has very favourable optical and mechanical properties and protects the motors from contamination and distortion. Finally, the microdrones are transferred into a water cell for actuation measurements (Fig. 4f and Supplementary Video 2).

2D control in all degrees of freedom

Despite their small size (Fig. 4f, diameter one-third of human red blood cells), the microdrones still reveal advanced capabilities. The results of actuation experiments for the two- and four-motor microdrones are presented in Figs. 5 and 6, respectively, and in Supplementary Videos 3–5. We find that the fundamental degrees of freedom of the control described in Fig. 3 are very well realized for both the two-motor (rotation and forwards–backwards translation in Fig. 5a,c, respectively) and the four-motor microdrones (rotation, forwards–backwards translation and right–left translation in Fig. 6a,b,c, respectively). Both translation and rotation are affected by noticeable random position and orientation fluctuations, which are attributed to Brownian motion of the microdrones caused by collisions with surrounding water molecules. Influence of thermal effects can be excluded here since the temperature increase at the microdrone body due to heating of the nanomotors is very small and symmetric[15].

The angular velocities of the rotations of several two-motor microdrones at various light powers have been extracted from corresponding videos. Figure 5b shows the plot of angular velocity as a function of the intensities of the two wavelengths. Because the microdrones do not always stay in the centre of the illumination spot, for each wavelength, the intensity is taken as the mean value in the region of the full-width at half-maximum of the illumination spot. Theoretical angular velocities calculated from a model considering viscous friction (Supplementary Note 2) at corresponding intensities are also plotted for comparison. It can be seen that the experimental angular velocities match the theoretical ones up to a factor of 1/3–1/2. For the linear motions, the velocities extracted from the videos are about 8 nm ms^{-1} at average intensities of about 0.3 mW μm^{-2} for both wavelengths. There is also a mismatch of a factor of about two between the measured translation velocities and the prediction, in agreement with the rotation case. We suspect that the observed mismatch is due to underestimated liquid drag in the model at very small length scales and increased viscosity of the liquid, as explained in Supplementary Note 2. It is important to note that the illumination intensities used here for driving the microdrones are orders of magnitude lower than those of conventional optical tweezers. Using low illumination intensity is an advantage for applications where sensitive (absorbing) materials or measurements are involved. As an example, the red blood cell in Fig. 4f has

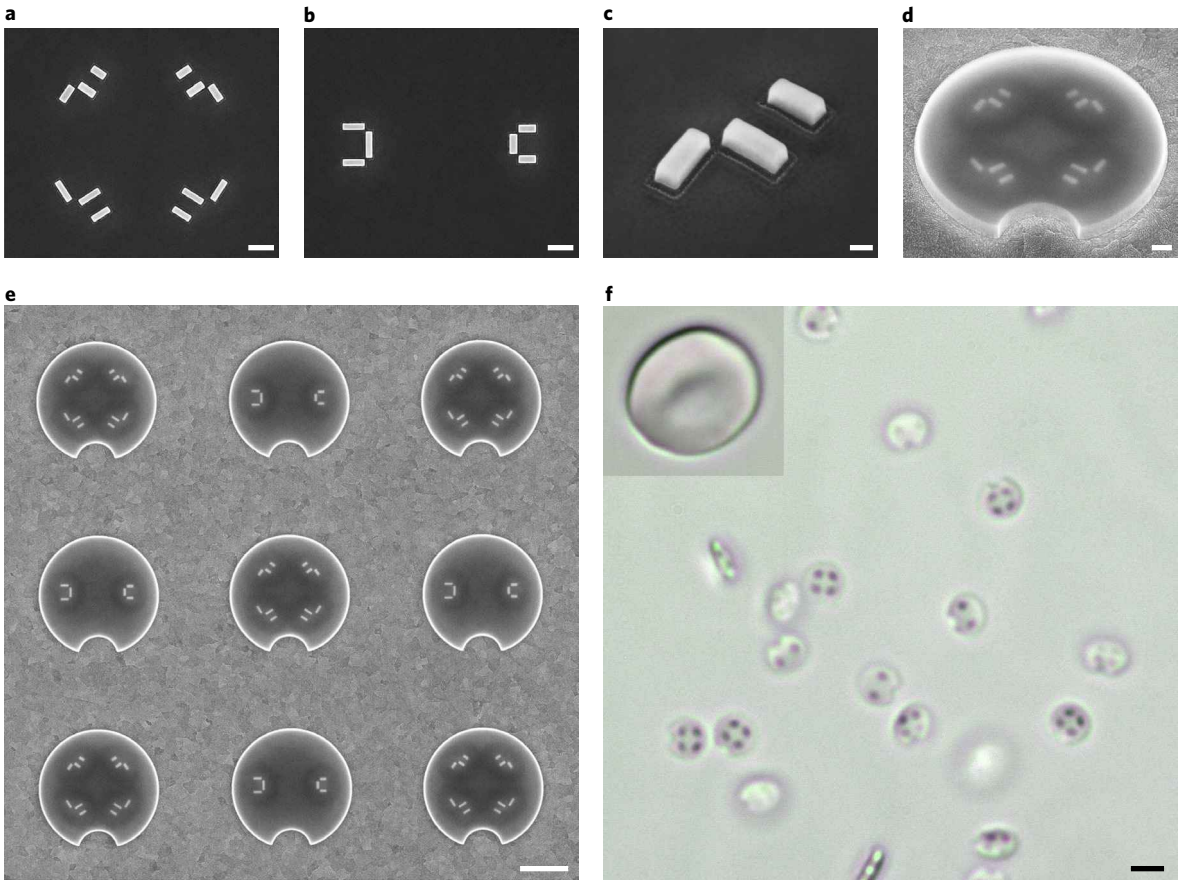

Fig. 4 | Scanning electron (a–e) and optical (f) micrographs of the fabricated structures. a,**b**, Top view of the gold nanomotors of the four- (**a**) and two-motor (**b**) microdrones still attached to the substrate. Scale bars, 200 nm. **c**, 40° tilt view of one of the nanomotors, showing the well-defined geometry of the structure. Scale bar, 50 nm. **d**, 40° tilt view of a completed microdrone on ITO substrate. The gold nanomotors are encapsulated in a circular disc that is produced using electron beam lithography and etching. Scale bar, 200 nm. **e**, Top view of an array of four- and two-motor microdrones on ITO substrate ready to be released. Scale bar, 1 μm. **f**, Microdrones released into a water cell in absence of the steering light field. Scale bar, 2 μm. The inset is an optical micrograph of a human red blood cell (same scale as the microdrones).

been illuminated with intensities also used for driving the microdrones but still sustains a good shape.

In addition to the basic motions, we also demonstrate steering of the microdrones along complex paths (Figs. 5d,e and 6d,e) using simple control schemes (Methods). An 8-shaped path is achieved by increasing or decreasing the power ratio between the two colours at some points, such that the microdrones turn to the right or left as required. A spiral path for the two-motor microdrone is implemented by gradually increasing the power ratio between the 830 and 980 nm light starting from 0, leading to a 'right turn' with increasing radius. For the four-motor microdrone, a spiral path is implemented by gradually increasing the power ratio between the CW and CCW components of the 830 nm light starting from zero, such that the microdrone turns to the left with an increasing radius. The drone orientation along the trajectories can be identified by means of the orange and red dots in the figures, which indicate the positions of the 830 and 980 nm motors, respectively (Methods). Note that, different from the two-motor microdrone that always moves 'forwards' in both the 8-shaped and the spiral paths (Supplementary Video 3), the four-motor microdrone moves 'leftwards' in the 8-shaped path but forwards in the spiral path (Supplementary Video 4), highlighting the additional degree of freedom for the four-motor microdrone.

Discussion

The actuation and nanomotor concept presented here can be extended to microdrones that are controlled in all six degrees of freedom of three-dimensional motions. To this end, counterpropagating beams should be used for illumination and new motor structures should be introduced to create out-of-plane forces that are dependent on the wavelength and circular polarization[44], such that the additional three degrees of freedom for out-of-plane motions can also be controlled, but without increasing the number of light sources. The direct and deterministic relation between light field properties and the resulting forces in three or six independent degrees of freedom in two or three dimensions in principle also enables a suppression of Brownian motion to a large degree, provided that corresponding feedback loops are implemented[45]. Feasibility of the necessary precise detection of the position and orientation of the microdrone has been demonstrated in Supplementary Videos 3 and 4. A rough estimation suggests that the position noise due to Brownian motion can be suppressed to below 10 nm using a feedback loop of 10 kHz bandwidth (Supplementary Note 3). Under such conditions, a microdrone could not only be steered along a desired path with very high precision, but also be stabilized at a certain position and orientation, analogous to optical trapping.

Conclusions

We have experimentally demonstrated light-driven microdrones. These miniature robotic devices contain up to four plasmonic nanoantennas as thrust motors based on directional light scattering, that is, photon recoil. The nanomotors can be addressed individually and directly by different circular polarization components of

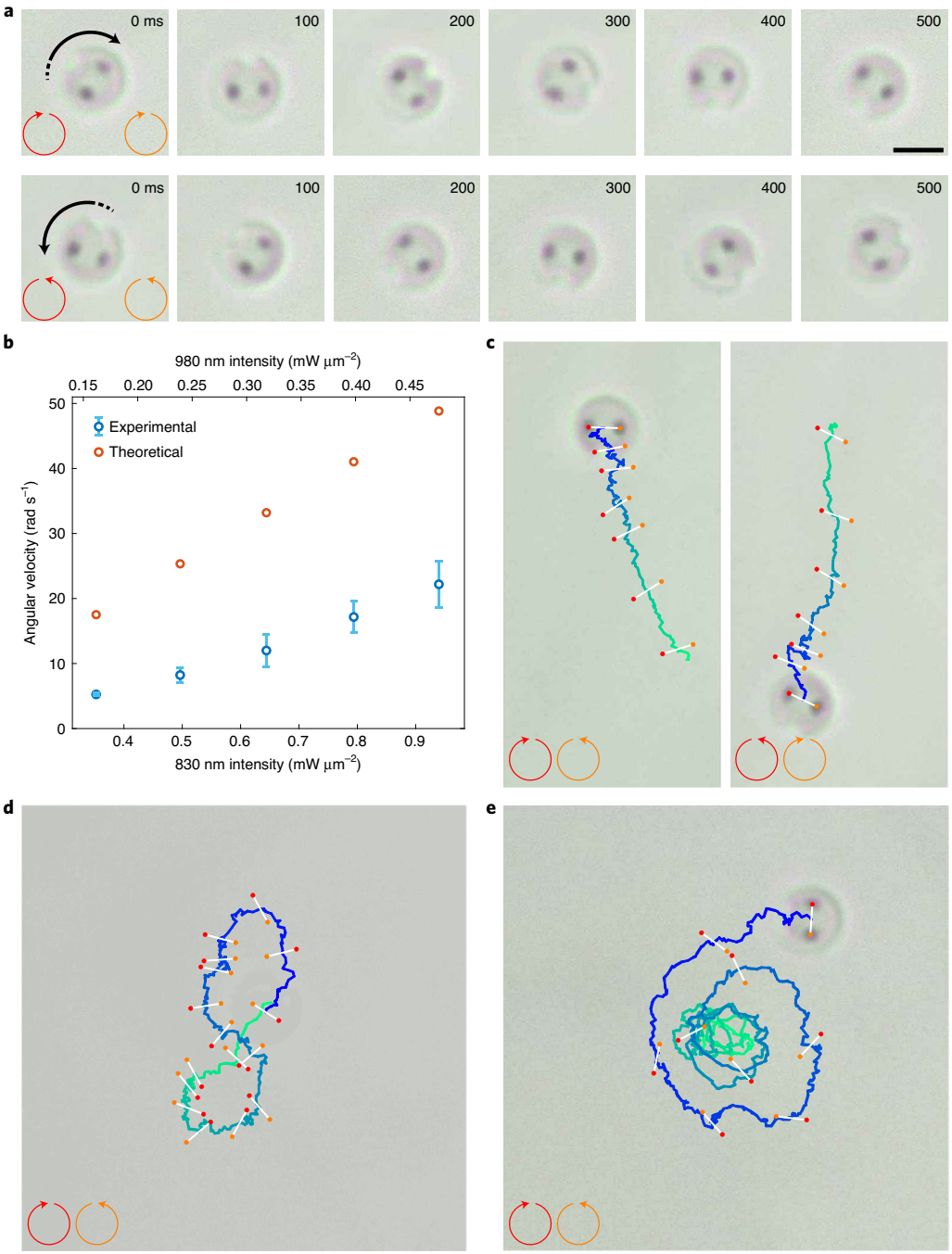

Fig. 5 | Actuation experiments of two-motor microdrones. a, Rotation in both CW and CCW directions (denoted by black arrows). The time interval between two adjacent snapshots is 100 ms. The images in each row show the same position on the sample. The scale bar (2 μm) applies to the whole figure. **b**, Measured (blue circles with standard deviation error bars) and theoretical (red circles) angular velocity in dependence of excitation intensities of the 830 and 980 nm light. **c**, Forwards–backwards translation. The two panels are for the same position on the sample and are continuous in time. **d**, Motion in an 8-shaped path. **e**, Motion in a spiral path. The motions are progressing in time from green to blue along the trajectories. The orange and red dots indicate the positions of the 830 and 980 nm motors, respectively, on every 25th (**c**) or 50th (**d** and **e**) frame (counting from the end frame, 1 frame corresponds to 10 ms). The white lines connecting the red and orange dots are guides for eye and represent the orientation of the microdrone. The orange and red circular arrows denote the circular polarizations of the 830 and 980 nm light, respectively. The laser spots of both lasers have a $1/e^2$ width of around 15 μm and are stationary. The mean intensities in **a** and **c** are around 0.31 and 0.15 mW μm^{-2} for 830 and 980 nm, respectively. The corresponding videos are found in Supplementary Video 3.

unfocused light fields of two wavelengths. Manoeuvring is realized by simply adjusting the respective power of the light field component that addresses each motor. The microdrones so far can be steered in all three degrees of freedom in two dimensions, but the concept can be extended to three dimensions, resulting in control of all six degrees of freedom. Steering in all independent degrees of freedom would allow stabilization of position and orientation as well as the motion of the microdrones through automated feedback control. Owing to their unique properties, light-driven microdrones may serve as a new experimental platform for many intriguing

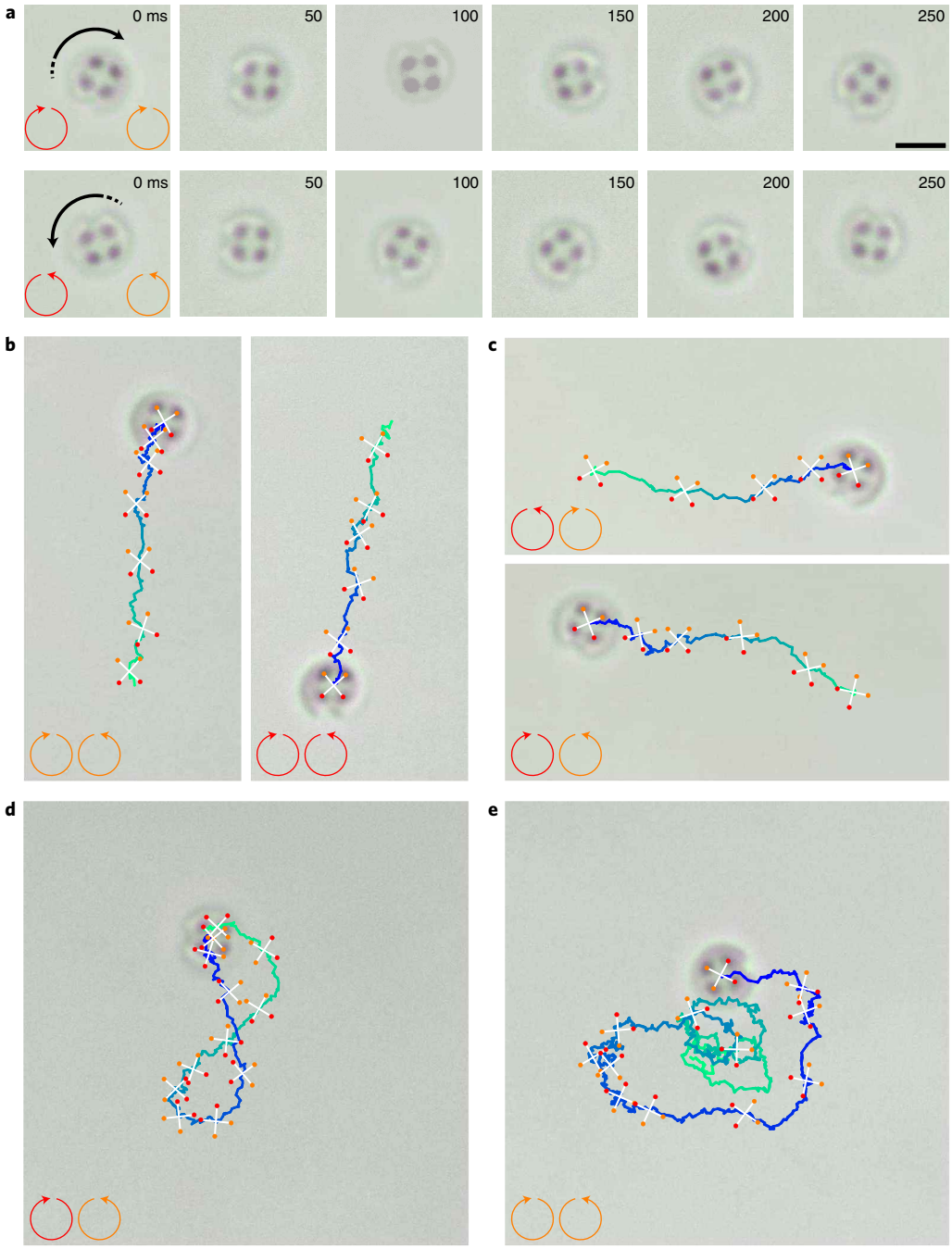

Fig. 6 | Actuation experiments of four-motor microdrones. a, Rotation in both CW and CCW directions (denoted by black arrows). The time interval between two adjacent snapshots is 50 ms. The images in each row show the same position on the sample. The scale bar (2 μm) applies to the whole figure. **b**, Forwards–backwards translation. **c**, Left–right translation. The two panels in **b** and **c** are for the same position on the sample and are continuous in time, respectively. **d**, Motion in an 8-shaped path. **e**, Motion in a spiral path. The motions are progressing in time from green to blue along the trajectories. The orange and red dots indicate the positions of the 830 and 980 nm motors, respectively, on every 25th (**b** and **c**) or 50th (**d** and **e**) frames (counting from the end frame, 1 frame corresponds to 10 ms). The white lines connecting the red and orange dots are guides for eye and represent the orientation of the microdrone. The orange and red circular arrows denote the circular polarizations of the 830 and 980 nm light, respectively. The laser spots of both lasers have a $1/e^2$ width of around 15 μm and are stationary. The mean intensities in **a**–**c** are around 0.31 and 0.22 mW μm^{-2} for 830 and 980 nm, respectively. The corresponding videos can be found in Supplementary Video 4.

applications. For instance, functional loads, such as tips[28,46], nanosensors[47] and plasmonic tweezers[31], as well as chemical cargos[48], could be attached to the microdrones, to perform interactive manipulation, scan-probing of cells and nano-objects, sensing of local environments, assembly of nano structures and transport of materials. Apart from the straightforward manipulation and delivery applications, combinations with plasmonic elements would be particularly attractive, as they can be directly incorporated into the present fabrication process. A good example is combination with plasmonic nanotweezers, which are useful for trapping nanoparticles but typically fixed on a substrate. A movable plasmonic tweezer could be obtained by fabricating the tweezer structure on

a microdrone. The low excitation intensity for microdrones also fits the requirements for plasmonic tweezers. Another example is tip-enhanced Raman scattering[46]. As a microdrone can be precisely manoeuvred and stabilized with help of feedback control, it can act as a remote scanning device in a liquid environment. A sharp gold tip could therefore be built on the microdrone to scan a liquid–solid interface and analyse the components by tip-enhanced Raman spectra. Similarly, other units such as plasmonic refractive index sensors or catalytic nanoparticles could also be integrated onto microdrones.

Online content

Any methods, additional references, source data, extended data, supplementary information, acknowledgements, peer review information; details of author contributions and competing interests; and statements of data and code availability are available at https://doi.org/10.1038/s41565-022-01099-z.

Received: 1 November 2021; Accepted: 16 February 2022;
Published online: 21 April 2022

References

1. Ashkin, A. Applications of laser radiation pressure. *Science* **210**, 1081–1088 (1980).
2. Cohen-Tannoudji, C. Manipulating atoms with photons. *Phys. Scr.* **T76**, 33–40 (1998).
3. Ashkin, A. Atomic-beam deflection by resonance-radiation pressure. *Phys. Rev. Lett.* **25**, 1321–1324 (1970).
4. Ashkin, A. Acceleration and trapping of particles by radiation pressure. *Phys. Rev. Lett.* **24**, 156–159 (1970).
5. Maragò, O. M., Jones, P. H., Gucciardi, P. G., Volpe, G. & Ferrari, A. C. Optical trapping and manipulation of nanostructures. *Nat. Nanotech.* **8**, 807–819 (2013).
6. Aspelmeyer, M., Kippenberg, T. J. & Marquardt, F. Cavity optomechanics. *Rev. Mod. Phys.* **86**, 1391–1452 (2014).
7. Ilic, O., Went, C. M. & Atwater, H. A. Nanophotonic heterostructures for efficient propulsion and radiative cooling of relativistic light sails. *Nano Lett.* **18**, 5583–5589 (2018).
8. Šípová-Jungová, H., Andrén, D., Jones, S. & Käll, M. Nanoscale inorganic motors driven by light: principles, realizations, and opportunities. *Chem. Rev.* **120**, 269–287 (2020).
9. Wang, J., Xiong, Z. & Tang, J. The encoding of light-driven micro/nanorobots: from single to swarming systems. *Adv. Intell. Syst.* **3**, 2000170 (2021).
10. Xin, H. et al. Optical forces: from fundamental to biological applications. *Adv. Mater.* **32**, 2001994 (2020).
11. Kawata, S. & Tani, T. Optically driven Mie particles in an evanescent field along a channeled waveguide. *Opt. Lett.* **21**, 1768–1770 (1996).
12. Wang, K., Schonbrun, E. & Crozier, K. B. Propulsion of gold nanoparticles with surface plasmon polaritons: evidence of enhanced optical force from near-field coupling between gold particle and gold film. *Nano Lett.* **9**, 2623–2629 (2009).
13. Brzobohatý, O. et al. Experimental demonstration of optical transport, sorting and self-arrangement using a 'tractor beam'. *Nat. Photon.* **7**, 123–127 (2013).
14. Búzás, A. et al. Light sailboats: laser driven autonomous microrobots. *Appl. Phys. Lett.* **101**, 041111 (2012).
15. Tanaka, Y. Y. et al. Plasmonic linear nanomotor using lateral optical forces. *Sci. Adv.* **6**, eabc3726 (2020).
16. Beth, R. A. Mechanical detection and measurement of the angular momentum of light. *Phys. Rev.* **50**, 115–125 (1936).
17. Friese, M. E. J., Nieminen, T. A., Heckenberg, N. R. & Rubinsztein-Dunlop, H. Optical alignment and spinning of laser-trapped microscopic particles. *Nature* **394**, 348–350 (1998).
18. Friese, M. E. J., Rubinsztein-Dunlop, H., Gold, J., Hagberg, P. & Hanstorp, D. Optically driven micromachine elements. *Appl. Phys. Lett.* **78**, 547–549 (2001).
19. Neale, S. L., MacDonald, M. P., Dholakia, K. & Krauss, T. F. All-optical control of microfluidic components using form birefringence. *Nat. Mater.* **4**, 530–533 (2005).
20. Tong, L., Miljković, V. D. & Käll, M. Alignment, rotation, and spinning of single plasmonic nanoparticles and nanowires using polarization dependent optical forces. *Nano Lett.* **10**, 268–273 (2010).
21. Lehmuskero, A., Ogier, R., Gschneidtner, T., Johansson, P. & Käll, M. Ultrafast spinning of gold nanoparticles in water using circularly polarized light. *Nano Lett.* **13**, 3129–3134 (2013).
22. He, H., Friese, M. E. J., Heckenberg, N. R. & Rubinsztein-Dunlop, H. Direct observation of transfer of angular momentum to absorptive particles from a laser beam with a phase singularity. *Phys. Rev. Lett.* **75**, 826–829 (1995).
23. Liu, M., Zentgraf, T., Liu, Y., Bartal, G. & Zhang, X. Light-driven nanoscale plasmonic motors. *Nat. Nanotech.* **5**, 570–573 (2010).
24. Yan, Z. & Scherer, N. F. Optical vortex induced rotation of silver nanowires. *J. Phys. Chem. Lett.* **4**, 2937–2942 (2013).
25. Galajda, P. & Ormos, P. Orientation of flat particles in optical tweezers by linearly polarized light. *Opt. Express* **11**, 446–451 (2003).
26. Rodrigo, P. J., Gammelgaard, L., Bøggild, P., Perch-Nielsen, I. R. & Glückstad, J. Actuation of microfabricated tools using multiple GPC-based counterpropagating-beam traps. *Opt. Express* **13**, 6899–6904 (2005).
27. Pollard, M. R. et al. Optically trapped probes with nanometer-scale tips for femto-Newton force measurement. *New J. Phys.* **12**, 113056 (2010).
28. Phillips, D. B. et al. An optically actuated surface scanning probe. *Opt. Express* **20**, 29679–29693 (2012).
29. Villangca, M. J., Palima, D., Bañas, A. R. & Glückstad, J. Light-driven micro-tool equipped with a syringe function. *Light: Sci. Appl.* **5**, e16148 (2016).
30. Lehmuskero, A., Li, Y., Johansson, P. & Käll, M. Plasmonic particles set into fast orbital motion by an optical vortex beam. *Opt. Express* **22**, 4349–4356 (2014).
31. Zhang, Y. et al. Plasmonic tweezers: for nanoscale optical trapping and beyond. *Light: Sci. Appl.* **10**, 59 (2021).
32. Chen, J., Ng, J., Lin, Z. & Chan, C. T. Optical pulling force. *Nat. Photon.* **5**, 531–534 (2011).
33. Song, J.-H., Shin, J., Lim, H.-J. & Lee, Y.-H. Optical recoil of asymmetric nano-optical antenna. *Opt. Express* **19**, 14929–14936 (2011).
34. Vercruysse, D. et al. Unidirectional side scattering of light by a single-element nanoantenna. *Nano Lett.* **13**, 3843–3849 (2013).
35. Andrén, D. et al. Microscopic metavehicles powered and steered by embedded optical metasurfaces. *Nat. Nanotech.* **16**, 970–974 (2021).
36. Wang, S. B. & Chan, C. T. Lateral optical force on chiral particles near a surface. *Nat. Commun.* **5**, 3307 (2014).
37. Rodríguez-Fortuño, F. J., Engheta, N., Martínez, A. & Zayats, A. V. Lateral forces on circularly polarizable particles near a surface. *Nat. Commun.* **6**, 8799 (2015).
38. Sukhov, S., Kajorndejnukul, V., Naraghi, R. R. & Dogariu, A. Dynamic consequences of optical spin–orbit interaction. *Nat. Photon.* **9**, 809–812 (2015).
39. Biagioni, P., Huang, J.-S. & Hecht, B. Nanoantennas for visible and infrared radiation. *Rep. Prog. Phys.* **75**, 024402 (2012).
40. Hoffmann, G., Huang, H., Waslander, S. & Tomlin, C. Quadrotor helicopter flight dynamics and control: theory and experiment. In *Proc. AIAA Guidance, Navigation and Control Conference and Exhibit* AIAA 2007-6461 https://doi.org/10.2514/6.2007-6461 (2007).
41. Castillo, P., Lozano, R. & Dzul, A. Stabilization of a mini rotorcraft with four rotors. *IEEE Control Syst. Mag.* **25**, 45–55 (2005).
42. Lu, F., Lee, J., Jiang, A., Jung, S. & Belkin, M. A. Thermopile detector of light ellipticity. *Nat. Commun.* **7**, 12994 (2016).
43. Huang, J.-S. et al. Atomically flat single-crystalline gold nanostructures for plasmonic nanocircuitry. *Nat. Commun.* **1**, 150 (2010).
44. Ding, K., Ng, J., Zhou, L. & Chan, C. T. Realization of optical pulling forces using chirality. *Phys. Rev. A* **89**, 063825 (2014).
45. Cohen, A. E. & Moerner, W. E. Suppressing Brownian motion of individual biomolecules in solution. *Proc. Natl. Acad. Sci. USA* **103**, 4362–4365 (2006).
46. Shao, F. & Zenobi, R. Tip-enhanced Raman spectroscopy: principles, practice, and applications to nanospectroscopic imaging of 2D materials. *Anal. Bioanal. Chem.* **411**, 37–61 (2019).
47. Xavier, J., Vincent, S., Meder, F. & Vollmer, F. Advances in optoplasmonic sensors – combining optical nano/microcavities and photonic crystals with plasmonic nanostructures and nanoparticles. *Nanophotonics* **7**, 1–38 (2018).
48. Gao, W. & Wang, J. Synthetic micro/nanomotors in drug delivery. *Nanoscale* **6**, 10486–10494 (2014).

Publisher's note Springer Nature remains neutral with regard to jurisdictional claims in published maps and institutional affiliations.

© The Author(s), under exclusive licence to Springer Nature Limited 2022

Methods

Numerical simulation. The finite-difference time-domain algorithm (Lumerical FDTD Solutions) is used for the simulations. Optical forces are calculated from the Maxwell stress tensor of the fields. Parameter sweeps are used to optimize the geometry of the motor structures. Some example results are presented in Supplementary Fig. 4. The refractive indices of gold and HSQ are set as in ref. [49] and to $n = 1.4$, respectively. For the results in Fig. 2, the HSQ body is set to be infinitely large, but the deviation of the results from the realistic case, where the body is a 200-nm-thick disc in water, is negligible, as shown in Supplementary Fig. 5. All forces and torques in the paper (including the Supplementary Information) are time-averaged values.

Microdrone fabrication. Plasmonic nanomotors are fabricated from single-crystalline gold flakes using a unique approach (Extended Data Fig. 1) based on focused helium ion beam milling (Zeiss Orion NanoFab). Gold flakes are chemically synthesized on glass coverslips[50] and a flake of the thickness matching the desired height of the motor structures is detached by a piece of polymethyl methacrylate (PMMA) and then transferred to the structuring substrate. The PMMA is dissolved by acetone before focused ion beam milling. The glass substrate features a thin layer of ITO and a layer of spin-coated HSQ on top. To define the desired motor structures, only the outlines (around 15 nm wide) of the structures are milled and the remaining gold material is removed by peeling off the gold flake. To peel off the gold flake without harming the motor structures, a droplet of polyvinyl alcohol (PVA) solution is deposited towards the right side of the gold flake to cover only one corner of the gold flake, leaving the motor structures untouched (lower image in Extended Data Fig. 1a). After drying out, the PVA piece acts as a handle for the gold flake, such that the gold flake can be peeled off by grabbing the PVA piece with a tweezer. It is seen that after gold flake peeling, the whole area is very clean and gold structures remain unaffected. This method reduces the patterning time tremendously and also drastically improves the resulting structure quality due to reduced proximity effect and redeposition of sputtered material. The body of the microdrone is created using electron beam lithography and HSQ etching (Extended Data Fig. 2).

The key steps of the transfer of microdrones into water are shown in Extended Data Fig. 3. To avoid losing the relatively small number of microdrones in water, the transfer approach takes advantage of the water solubility of PVA. The ITO layer is first etched using HCl, and the microdrones are then covered by a droplet of PMMA solution. After drying out, the PMMA piece is peeled off the substrate together with the microdrones. The PMMA piece is placed upside down on a substate with the microdrones on the upper side. Now a droplet of PVA solution is placed on the PMMA piece and covers the microdrones. Once the PVA droplet dries out, the PMMA-PVA compound is dipped into acetone to dissolve the PMMA layer. The microdrones are thus transferred to the PVA piece, which is then placed on a substrate with the microdrones on the upper side. To reduce the amount of PVA to enter the water cell, a small area (about 200 μm) of PVA containing the microdrones is cut out and moved onto the bottom coverslip of the water cell. Before closing the water cell, a water droplet is put onto the top coverslip, such that the PVA piece on the bottom coverslip is covered by the water droplet when the top coverslip is put into place. The PVA piece is then dissolved and the microdrones are released into the still water. As a result, the microdrones are swarming as a group and remain easy to find under microscope. Tiny amounts of sodium dodecyl sulfate (10 mM) and NaCl (5 mM) are added to the water to generate the same surface charging on both the microdrones and the substrate of the water cell, such that the microdrones do not stick to the substrate and a gap of a few hundreds of nanometres is maintained when the driving light is on.

Optical setup and measurement. A schematic of the optical setup is shown in Extended Data Fig. 4. The light sources are continuous wave laser diodes. The two beams are overlapped and focused to the back focal plane of the top objective to generate a large-area unfocused illumination. The polarization of the light is manipulated by manually moving in or out the half- and quarter-wave plates or rotating the quarter-wave plate (for Fig. 6e only). The output power of each laser diode is adjusted by controlling the laser diode current via a LabView program.

The positions of the motors of a microdrone in the videos are determined using a computer program that detects the dark spots representing the motors in every video frame and fits each spot with a 2D elliptical Gaussian function. The centre of the microdrone is extracted from the fitted motor coordinates. The original videos have a frame rate of 100 frames per second.

Data availability

The data for Fig. 5b are provided as source data with this paper. Other data supporting the conclusions of this study are available in the paper (including Supplementary Information).

Code availability

The codes used during this study are available from the corresponding authors upon reasonable request.

References

49. Johnson, P. B. & Christy, R. W. Optical constants of the noble metals. *Phys. Rev. B* **6**, 4370–4379 (1972).
50. Krauss, E. et al. Controlled growth of high-aspect-ratio single-crystalline gold platelets. *Cryst. Growth Des.* **18**, 1297–1302 (2018).

Acknowledgements

Financial support by the German Research Foundation (DFG grant no. HE5618/10-1) and the Volkswagen Foundation via an 'Experiment!' grant (both received by B.H.) is gratefully acknowledged.

Author contributions

B.H. and X.W. conceived the project. X.W. designed the devices, structures and experiments. X.W., G.R. and T.F. performed numerical simulations. X.W. fabricated the samples and constructed the optical setup. X.W., R.E. and J.Q. carried out the optical measurements and analysed the data. X.W. and B.H. wrote the manuscript. All authors contributed to the discussion and manuscript preparation.

Competing interests

The authors declare no competing interests.

Additional information

Extended data are available for this paper at https://doi.org/10.1038/s41565-022-01099-z.

Supplementary information The online version contains supplementary material available at https://doi.org/10.1038/s41565-022-01099-z.

Correspondence and requests for materials should be addressed to Xiaofei Wu or Bert Hecht.

Peer review information *Nature Nanotechnology* thanks Mikael Käll, Yun-Feng Xiao and the other, anonymous, reviewer(s) for their contribution to the peer review of this work.

Reprints and permissions information is available at www.nature.com/reprints.

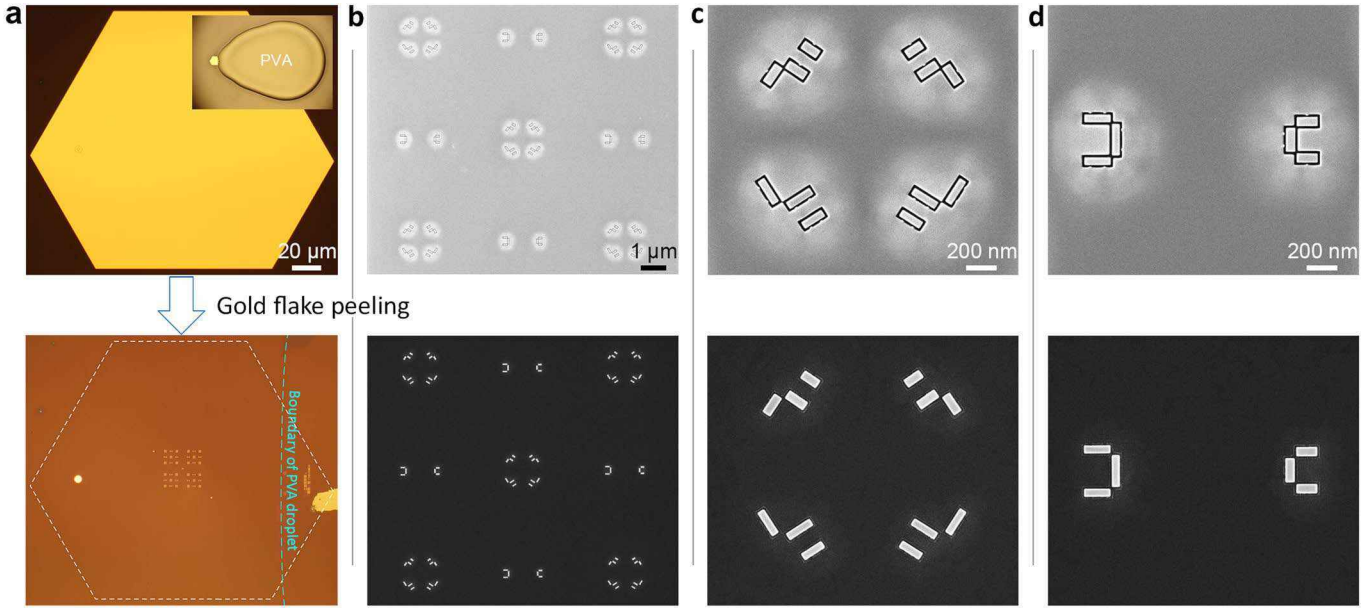

Extended Data Fig. 1 | Fabrication of the gold nanomotors. Upper row: Optical micrograph of a gold flake (**a**) and scanning helium ion micrographs of the nanomotor structures (**b**-**d**) after outline milling with focused helium ion beam. Lower row: Optical micrograph (**a**) and scanning electron micrographs (**b**-**d**) of the nanomotor structures after the gold flake is peeled off. The inset of the upper panel of **a** is an optical micrograph of the gold flake when its right corner is covered by a dried-out droplet of PVA solution. The outline of the gold flake and the boundary of the PVA droplet at the gold flake region are illustrate by the dashed lines in the lower panel of **a**.

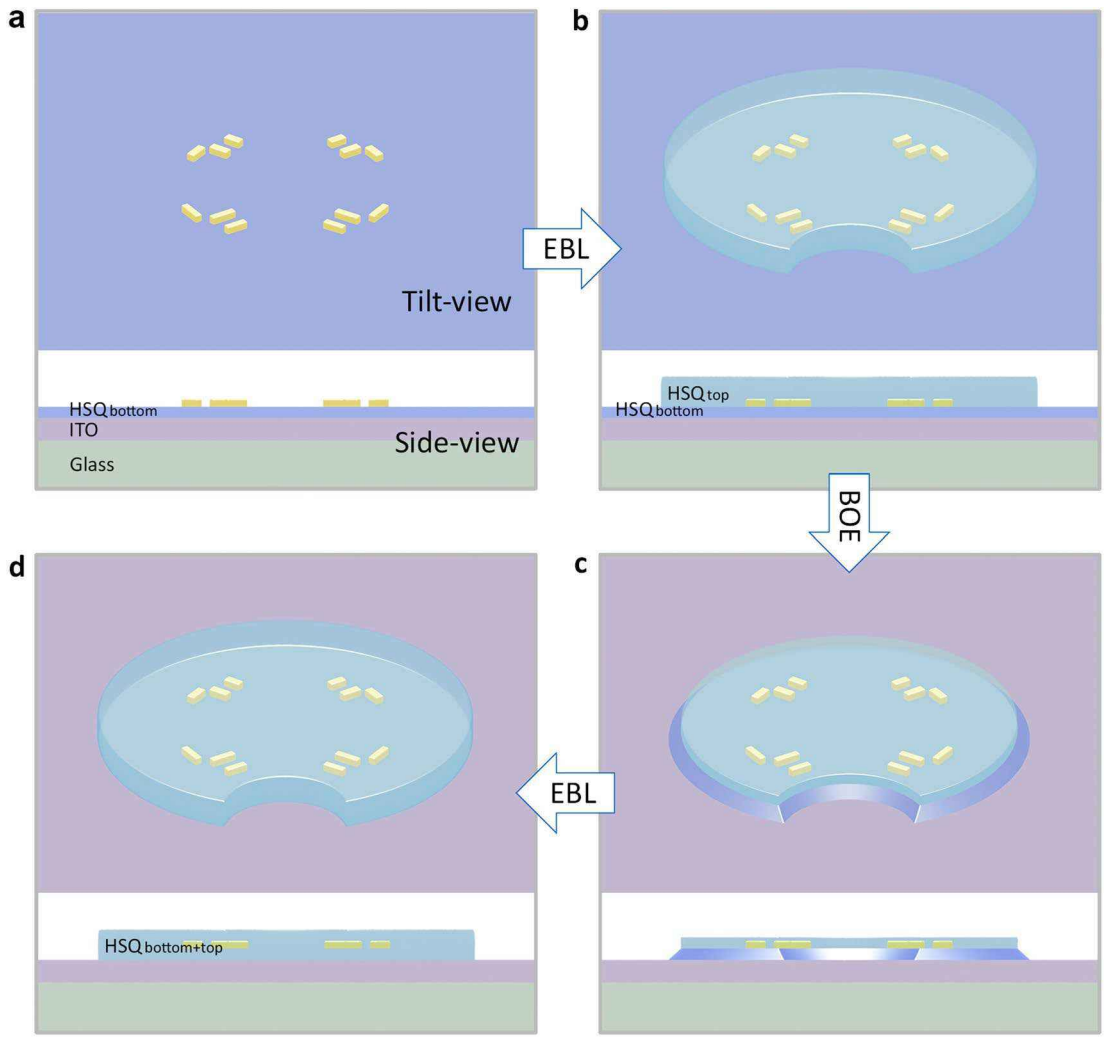

Extended Data Fig. 2 | Fabrication of the microdrone body. a, Gold nanomotors are fabricated on top of a spin-coated HSQ layer on an ITO/glass substrate. **b**, An etching mask of HSQ with the same shape of the microdrone body but increased thickness is created in the first electron beam lithography (EBL) step. **c**, The bottom HSQ layer is etched through with buffered oxide etch (BOE). The top mask is also thinned down and the wet etching leads to an unwanted side profile. **d**, The sample is spin-coated with HSQ again and the final body with defined shape and dimensions is created in the second EBL step. In panels **a**-**c**, the top and bottom HSQ layers are presented in different colors for better illustration.

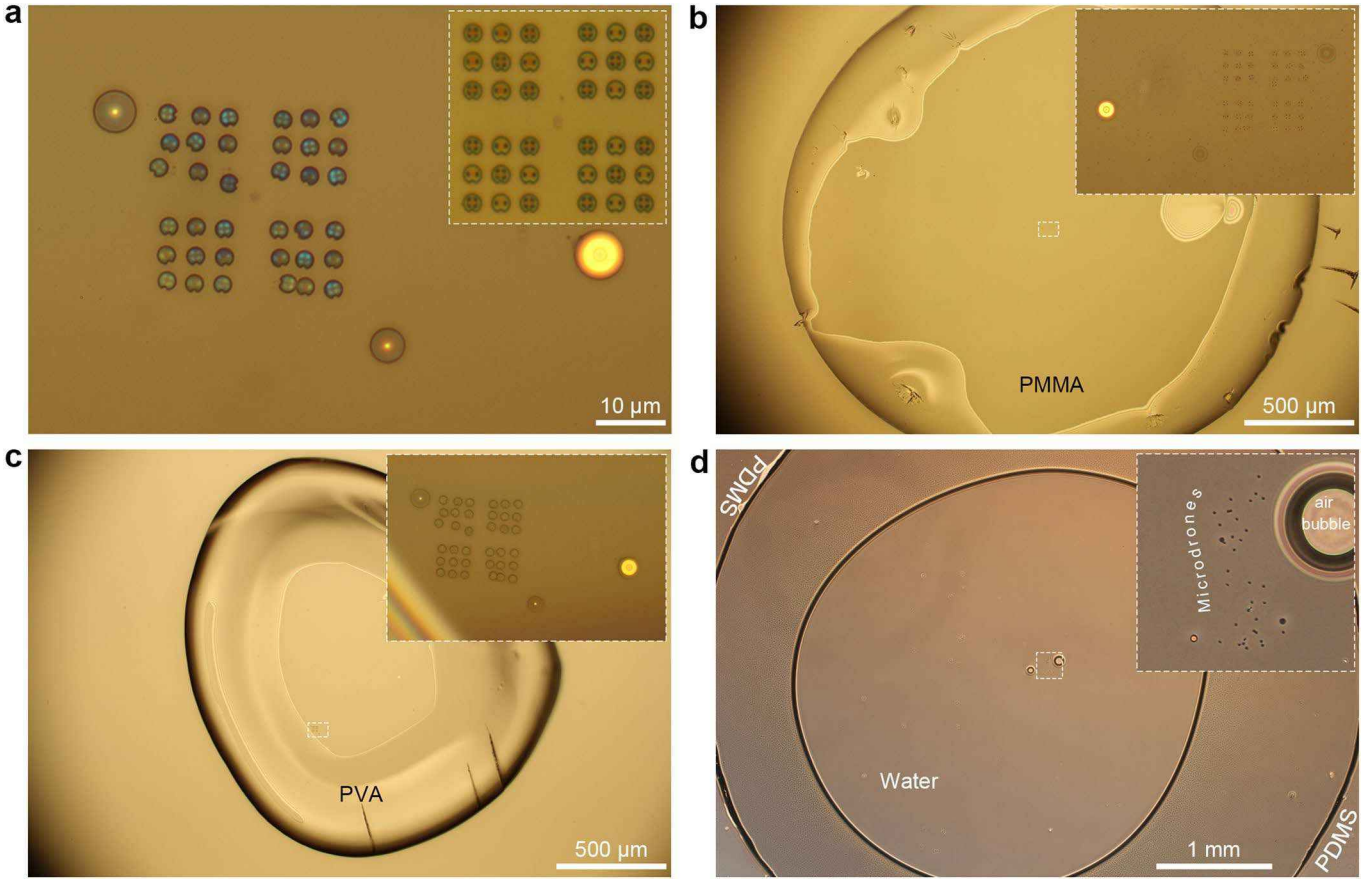

Extended Data Fig. 3 | Transfer of microdrones to a water cell. Reflection (**a**-**c**) and phase-contrast transmission (**d**) optical micrographs of microdrones of a sample at key steps of the transfer process. **a**, On the glass substrate after ITO etching. The microdrones have moved slightly after the etching. The inset shows the well-aligned array before ITO etching. The shiny dots and disk are gold markers for pattern alignment for electron beam lithography. **b**, A PMMA piece with the microdrones attached on the top. A zoom to the area indicated by the dashed rectangle is shown in the inset (same for **c** and **d** as well). It is seen that the microdrone array is right-left flipped as compared to **a**. **c**, A PVA piece with the microdrones attached on the top. The microdrone array is flipped again as compared to **b**. **d**, The microdrones are transferred to water. The water droplet has a volume of about 2.5 μL and is sandwiched between two glass coverslips with a spacer of PDMS (165 μm thick). Now the microdrones are seen as the swarm of dark dots. The air bubble to the right will disappear with time.

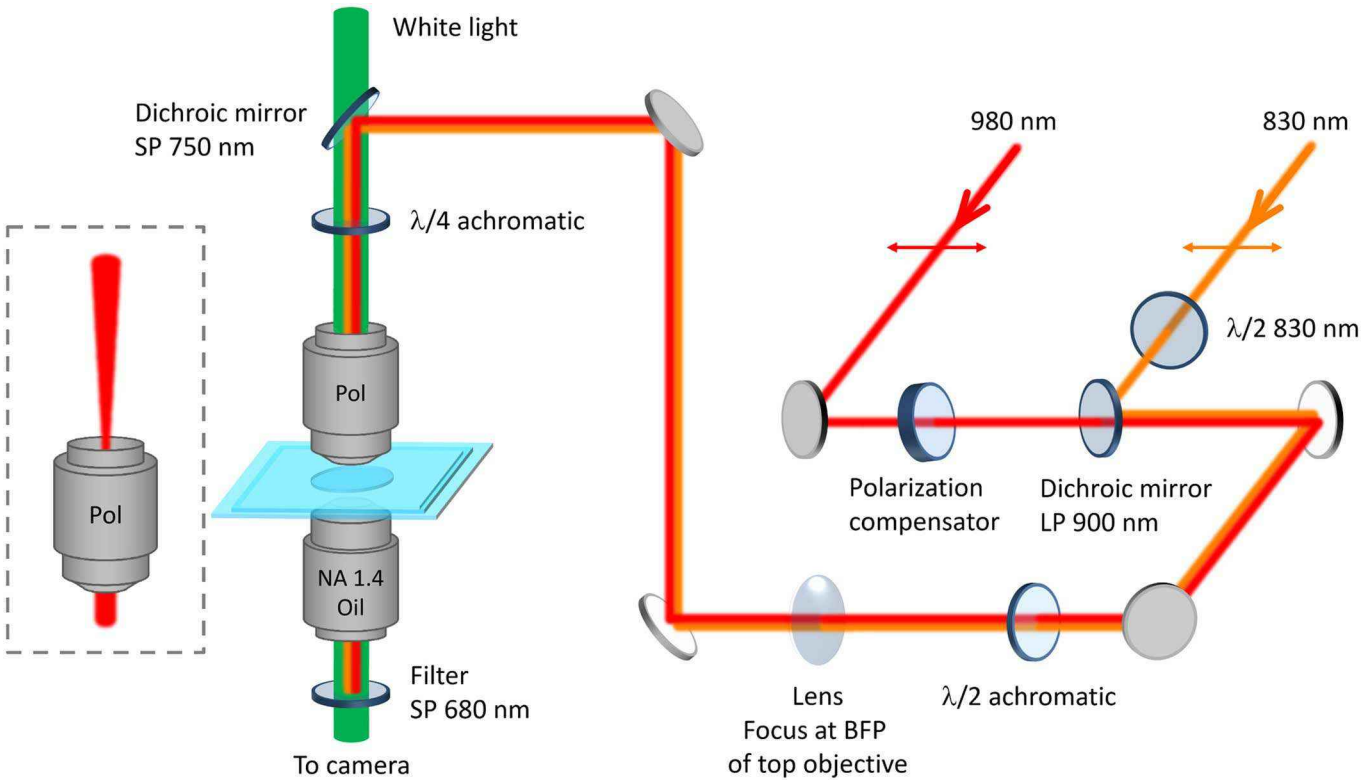

Extended Data Fig. 4 | Schematic of the optical setup. The inset to the left sketches the fact that both laser beams are focused by the lens to the back focal plane (BFP) of the top objective (for polarized light) to create unfocused light fields. Both 830 and 980 nm laser beams pass a polarizer (horizontal direction) positioned directly behind the laser diodes. The two light beams are overlapping after the dichroic mirror LP 900 nm. The polarization compensator is used to correct the influence of the dichroic mirror LP 900 nm to the linear polarization of the 980 nm beam. The components and the water cell are not to scale.